Research Article

$MnFe_2O_4/ZrO_2$ nanocomposite as an efficient magnetically separable photocatalyst with good response to sunlight: preparation, characterization and catalytic mechanism

S. Meena[1] · K. S. Anantharaju[2] · Y. S. Vidya[3] · L. Renuka[4] · S. Malini[2] · S. C. Sharma[5] · H. Nagabhushana[6]

Received: 1 July 2019 / Accepted: 21 January 2020 / Published online: 3 February 2020

Abstract
Magnetically separable novel nano-$MnFe_2O_4/ZrO_2$ nanocomposite (NC) and $MnFe_2O_4$ (MFO) samples were synthesized by an efficient solution combustion methodology. The structure, morphology and optical properties were characterized through powder X-ray diffraction, scanning electron microscopy, Fourier-transform infrared spectroscopy and UV–Vis spectroscopy. The photocatalytic activity of $MnFe_2O_4/ZrO_2$ nanocomposite was analysed for decolourization efficiency of methylene blue (MB) and textile dye wastewater under natural sunlight irradiation. The results demonstrated that the decolourization response of the $MnFe_2O_4/ZrO_2$ nanocomposite was 95% for MB and 59% for textile dye wastewater in 90 min. The photocatalytic performance of $MnFe_2O_4/ZrO_2$ was almost 1.4 times as high as pure $MnFe_2O_4$ was ascribed to the synergic effect and interfacial interaction across $MnFe_2O_4$ nanoparticle (NP) and ZrO_2 that leads to separation of electron–hole pairs efficiently and broadened light absorption of the composite (2.42 eV) compared to $MnFe_2O_4$ (2.15 eV). The effective optimized parameters such as solution pH of 7, nanocomposite dosage of 60 mg and initial dye concentration of 20 ppm were studied on photocatalytic performance for the removal of MB dye. The magnetically separable $MnFe_2O_4/ZrO_2$ nanocomposite proved to be highly active and a stable catalyst in five successive photodecolourization cycles for an aqueous solution of MB dye under sunlight irradiation. Furthermore, the possible sunlight photocatalytic mechanism of the $MnFe_2O_4/ZrO_2$ nanocomposite was proposed. Due to its enhancement in photocatalytic activity, this NC has great potential towards the environmental remediation for practical photocatalytic application towards wastewater treatment.

Keywords Magnetic nanocomposite · Combustion route · Photocatalytic performance · Synergic effect · Sunlight irradiation

1 Introduction

The existence of dyes in the present industrial effluents is a main concern as it is fatal to aquatic environment and humans. Many industries utilize organic dyes to colour their commodities and discharge considerable amount of coloured textile wastewater, often difficult to reprocess owing to the complicated aromatic structure of the dyes [1]. A cationic methylene blue (MB) dye extensively utilized in dying cotton, wood and silk causes permanent visual impairment in wild animals and humans [2]. Substantial research has been dedicated to thiazine dyes focusing on methylene blue with 37% of publications reporting on the photodegradation pathway of MB dye [3]. A variety of

✉ K. S. Anantharaju, iamananthkurupalya@gmail.com; ✉ Y. S. Vidya, vidyays.phy@gmail.com | [1]Department of Science, East West Institute of Technology, Bengaluru 560091, India. [2]Department of Chemistry, Dayananda Sagar College of Engineering, Bengaluru 560078, India. [3]Department of Physics, Lal Bahadur Shastri Government First Grade College, Bengaluru 560032, India. [4]Department of Chemistry, Rajalakshmi Engineering College, Thandalam, Chennai 602105, India. [5]National Assessment and Accreditation Council, Work Carried Out as Honorary Professor, Jain University, Bengaluru, India. [6]Prof. C.N.R. Rao Centre for Advanced Materials, Tumkur University, Tumkur 572 103, India.

methods such as adsorption process [4], sedimentation, chemical precipitation, oxidation [5], reduction, flocculation [6] and various biological ways are employed to rectify the problem caused by various dyes [7].

Adsorption is one of the most suited techniques extensively used to remove synthetic dyes from wastewater. However, conventional absorbents pose restrictions in their purpose such as low adsorption ability or regeneration of adsorbent. Porous crystalline metal–organic frameworks (MOFs) as adsorbent materials made of metal ions coordinated to organic ligands are an attractive option owing to their high surface area, easy separation, higher porosity, variety in structure and functionality. Magnetic Fe_3O_4 can be conveniently recycled from aqueous solution by the use of an external magnet. The build of magnetic nanocomposites firmly supports easy adsorption and recycling. Often, MOFs synthesis and utilization require a lengthy process of centrifugation, which restricts its scope, particularly in tailoring the growth of MOF on magnetic nanomaterials [8].

Some ligand-based nanocomposite adsorbents are recently utilized for the removal of specific ions like Cerium (III) [9], Pb^{2+} [10], Selenium (IV) [11], Pd^{2+} [12] [13], Cu^{2+} ions [14, 15], phosphate [16] and nitrite ion [17]. The preparation and regeneration of the core material in these composites for the adsorption of specific metal ions consume more time and economically not viable. NiS/CDs/CdS composite photocatalysts were designed and successfully synthesized for high-efficient hydrogen evolution [18]. Nanocomposite of three-dimensional carbon dots decorated Bi/titanium dioxide [19] and core-shelled $CeO_{2-x}S_x$@CdS ternary composite [20] is also prepared and employed for the degradation of RhB under sunlight, but for an uncomplicated regeneration, the latter said composites are least possible. The photocatalysis is an attractive and alternate substitute in the environmental engineering process and can be scaled up in industries [21]. Its main advantages are its low cost, stability, environmental friendliness, renewable energy consumption (Sun), a high degree of mineralization [22] and its ability to remove a variety of industrially important organic pollutants.

Spinel magnetic ferrites (MFe_2O_4: M = Zn, Ca, Co, Mn, Mg, Ni, etc.) are considered to be very important in the field of material science and nanotechnology due to its chemical stability, high reactivity and reusability. This magnetic ferrite NP can be recycled and reused for several cycles during photocatalysis due to its chemical stability [23]. It shows better performance in catalytic/photocatalytic activity because of its narrow band gap of approximately 2.0 ± 0.5 eV [24]. However, enhanced photocatalytic activity cannot be achieved due to its narrow band gap. Among the ferrites, MFO is considered to be a potential material due to its versatile applications possessing high saturation magnetization, better magnetic properties, chemical stability [25], high surface area, high saturation and high mechanical hardness and is specifically used as a semiconductor photocatalyst for environmental remediation [26]. Despite its resourceful properties and applications, its photocatalytic activity towards dye degradation was found to be less due to its narrow band gap that leads to electron–hole pair recombination. Hence, many researchers have made an attempt to combine wide band gap semiconductors with these narrow band gap ferrites to achieve an excellent photocatalytic activity [27]. Generally, preparing an appropriate hetero-junction between $MnFe_2O_4$ and metal oxide is considered as a better option to inhibit electron–hole pairs recombination and to improve photocatalytic efficiency.

Many metal oxides were recognized as suitable photocatalysts due to its ability of efficiently removing organic pollutants from the waste polluted water. Out of the available metal oxides, ZrO_2 was chosen as the semiconductor nanomaterial to prepare NC with MFO due to its wide band gap, high persistence and good tendency to degrade the organic pollutants in wastewater [28]. ZrO_2 is a highly efficient photocatalyst towards the degradation of dyes under UV light, but it fails towards solar light due to its wide band gap. Hence, by combining ZrO_2 with narrow band gap semiconductor, photocatalytic activity can be enhanced. There are many reports available for the synthesis of NC with $MnFe_2O_4$ for many applications such as $MnFe_2O_4$/rGO NC for ultra-stable supercapacitors [29], ZnO/$MnFe_2O_4$ synthesis by organic-free media for dye degradation under natural sunlight [30], $MnFe_2O_4/ZrO_2$ by sol–gel method for sonocatalytic and photocatalytic degradation of methylene blue and methyl orange dye under UV–visible light [31], $MnFe_2O_4$/g-C_3N_4/TiO_2 NC generated by chemical impregnation method for degradation of methyl orange dye simulated under irradiation of solar light [32], magnetic microsphere $MnFe_2O_4$/polyaniline composite with electro-catalytic activity for oxygen reduction reaction [33] and $MgFe_2O_4/ZrO_2$NC [34] by modified citrate gel method for hyperthermia applications.

This NC can be synthesized with different structures by various methods such as sol–gel, polyol, solvothermal, hydrothermal, co-precipitation and ball milling [35–38]. Though advantageous, these strategies have drawbacks like energy overriding, higher temperature requirement and complicated apparatus. Also, the formation of final products with better crystallization may take longer time to complete [39]. Here, an attempt has been made to synthesize MFO/ZrO_2 by solution combustion method, due to its advantages such as less time consumption for synthesis, energy efficiency, simple apparatus requirement, mixing of raw materials at a molecular level, tuneable product

composition, efficient, economical and homogeneity preparation of industrial metal oxide semiconductor [40].

The examination of the physico-chemical characterization and the associated electro-chemical activity of the composite confirmed the photocatalytic activity benefits due to synergistic modulation of the photoabsorption, improved photoredox capability and enhanced adsorption capacity. The current work mainly focuses on evaluating the decolourization kinetics of MB dye and textile wastewater under sunlight at hetero-structure MFO/ZrO_2 photocatalyst. The study also reveals the effective optimized parameters being pH, initial concentration of dye and the catalyst. Photocatalytic decolourization and probable pathways for the decolourization of MB dye pollutant in wastewater are demonstrated. The findings hopefully are worthy and helpful and set a foundation for the development of hetero-structured ferrite nanocomposite photocatalysts to deal with the environmental challenges and issues in developing the process technology.

2 Materials and methods

Highly pure analytical grade manganese nitrate $Mn(NO_3)_2$, iron(III) nitrate [$Fe(NO_3)_3$. $9H_2O$] and zirconyl oxynitrate ($ZrO(NO_3)_2$) with 99% purity were procured from Merck, Co. Hence, further purification procedures were excluded.

2.1 Photocatalyst preparation

2.1.1 Synthesis of $MnFe_2O_4$NP

MFO was prepared through solution combustion method using an oxidizer constituting a mixture of manganese nitrate Mn $(NO_3)_2$ and iron(III) nitrate (Fe $(NO_3)_3$·$9H_2O$) with laboratory-synthesized ODH as an efficient fuel. A mixture of fuel and oxidizer in a stoichiometric ratio was transferred into a cylindrical crucible with addition of small quantity of water and blended to get a homogeneous mixture. The crucible was put into a preheated muffle furnace with a temperature of 500 °C. The resulting solution was initially boiled and subsequently dehydrated with elimination of gases like carbon dioxide, nitrogen and water vapour followed by the formation of the sample.

2.1.2 Synthesis of MFO/ZrO_2 NC

To obtain MFO/ZrO_2NC, a combination of manganese nitrate [$Mn(NO_3)_2$], ferric (III) nitrate [(Fe $(NO_3)_3$. $9H_2O$)] and zirconyl oxynitrate [($ZrO(NO_3)_2$)] was carefully mixed in stoichiometric ratio with addition of fuel. A repetition of the above said procedure leads to the synthesis of MFO/ZrO_2 NC as depicted in Fig. 1.

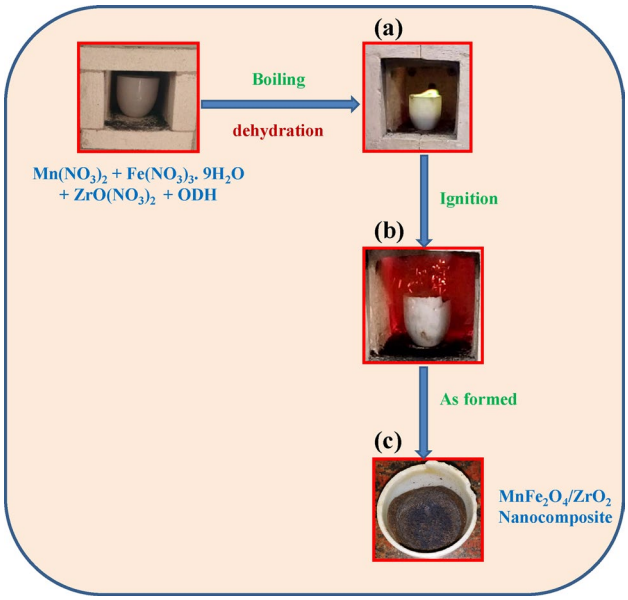

Fig. 1 Typical combustion procedure. (a) Initial stage before combustion starts; (b) ignition liberation of gases during the combustion process; (c) final product (MFO/ZrO_2 NC)

3 Characterization

The morphology associated with the surface area of the synthesized samples has been noted with the aid of SEM, Hitachi-3000. PerkinElmer FTIR (Spectrum-1000) spectrometer was used in detecting the important functional groups within a scan range of 4000–400 cm^{-1}. Adsorption was measured using ELICO UV–Vis spectrophotometer (SL159). Phase purity of all synthesized sample was identified using X-ray diffraction of powder (PXRD) patterns noted employing a Shimadzu 7000 diffractometer with CuKα radiation with a 2^o min^{-1} of scan rate.

3.1 Results and discussion

3.1.1 Powder X-ray diffraction analysis

The PXRD spectra of MFO and MFO/ZrO_2 NC are depicted in Fig. 2a. The XRD results of MFO show crystalline with specific peaks at 2θ values 30° (202), 35.23° (311), 43° (400), 53.4° (422), 56.73° (333) and 62.30° (440) analog to the spinel cubic structure and Fd3m space group (JCPDS card No. 75-0034) [41]. PXRD pattern of MFO/ZrO_2 NC depicts the peaks at 50.87° and 60.48° corresponding to (112) and (121) plane of tetragonal ZrO_2 (JCPDS card NO. 81-1544) in addition to MFO peaks. The presence of characteristic peak corresponding to MFO and ZrO_2 without any additional peak confirms the formation of NC. The broadening and shifting of peaks towards higher angle are observed in MFO/ZrO_2 NC indicating a minor variation in lattice

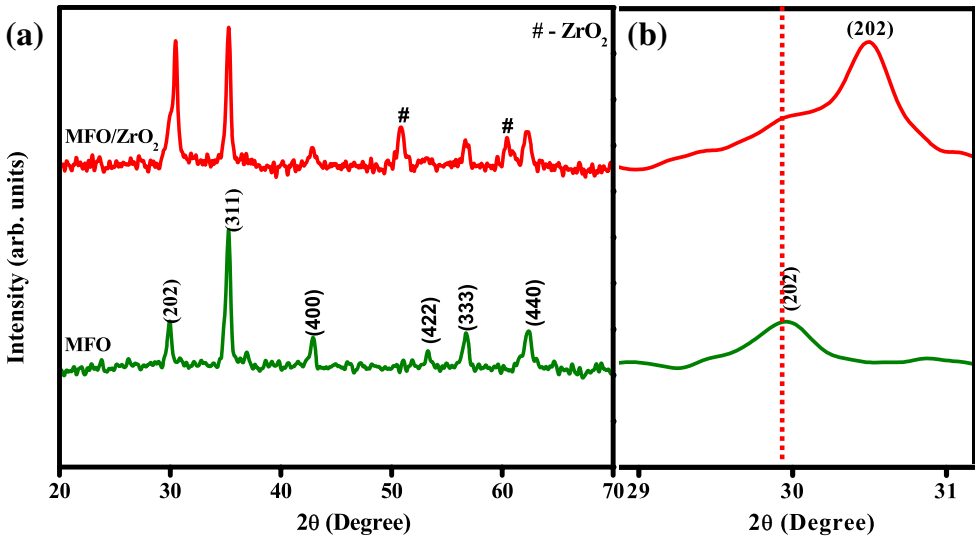

Fig. 2 PXRD pattern of **a** synthesized MFO and MFO/ZrO_2 NC, **b** shifting of (202) PXRD peak towards higher angle side

constant (Fig. 2b). The observed variation in lattice constant was due to the partial replacement of Zr^{4+} cation at Mn^{2+} site. The intensity of NC is high compared to host matrix.

The crystallite size was quantified by Scherrer's formula using half-width of the prominent peak of maximum intensity (311) plane. The results depict that the crystalline size of host is 16 nm and that of MFO/ZrO_2 NC is 18 nm. The crystalline size of NC was found to be increased compared to that of host sample. The W–H approach recognizes the case when the domain effect and lattice deformation both operate simultaneously and their combined effects give the final line broadening FWHM (β), which is the sum of grain size and lattice distortion. The effects of strain and crystallite size on the FWHM are predicted using Williamson–Hall plots [42]. The grain size for MFO and MFO/ZrO_2 NC was found to be 17 and 19 nm. The negligible variation in the values arises from the fact that in Scherrer's formula, strain component was assumed to be zero and observed that broadening of diffraction peak was due to increasing grain size only. As the crystallinity increases, the photocatalytic property of the sample will increase [43].

Table 1 shows the quantified crystallite size, dislocation density and stacking fault. Some other crucial structural parameters, for instance the dislocation density due to ionic stress and stacking fault, were quantified utilizing the equations [44, 45].

$$\delta = \frac{1}{D^2} \tag{1}$$

$$\mathrm{SF} = \left[\frac{2\pi^2}{45\,(3\tan\theta)^{1/2}}\right] \tag{2}$$

3.1.2 Morphological studies

Figure 3a, b represents the FESEM images of MFO and MFO/ZrO_2 NC. As can be seen from the images, the crystallites are uneven in shape and hold several voids and pores (shown in the form of circles) due to the escaping gases during combustion synthesis. The voids are more in host matrix, and small size pores are observed in MFO/ZrO_2 NC. Besides that, agglomeration that was observed could be due to magnetic properties of the compound [46]. This kind of voids and porous nature is a normal characteristic of combustion-synthesized powders [47].

3.1.3 FTIR studies

The FTIR spectra of the synthesized MFO and MFO/ZrO_2 NC at room temperature are illustrated in Fig. 4. The characteristic peak observed below 1000 cm^{-1} is the general feature of ferrites. The characteristic peak observed at 545 and 523 cm^{-1} in MFO and MFO/ZrO_2 NC correlates with

Table 1 Estimated crystallite size and other structural parameters of MFO and MFO/ZrO_2

Samples	FWHM (β) (rad)	Crystallite size (nm)		SF	δ (10^{15} lin m^{-2})	Band gap (eV)
		D–S method (nm)	W–H plots (nm)			
MFO	0.446	16	17.4	0.4646	2.74	2.15
MFO/ZrO_2	0.45	18	18.5	0.4677	2.89	2.42

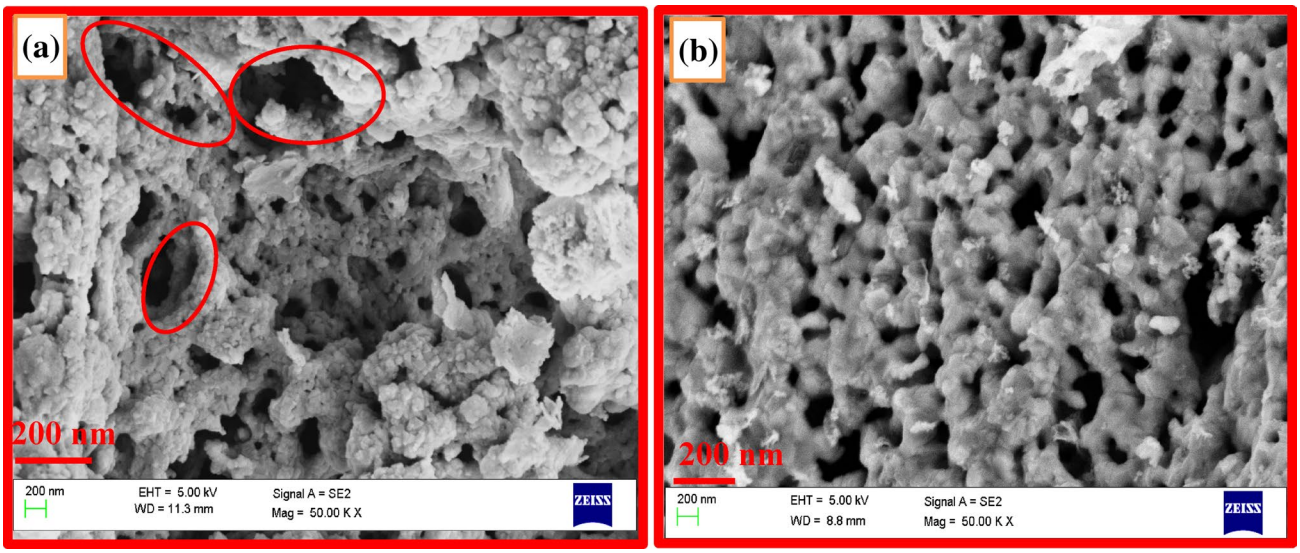

Fig. 3 SEM image of **a** synthesized MFO NP; **b** MFO/ZrO_2 NC

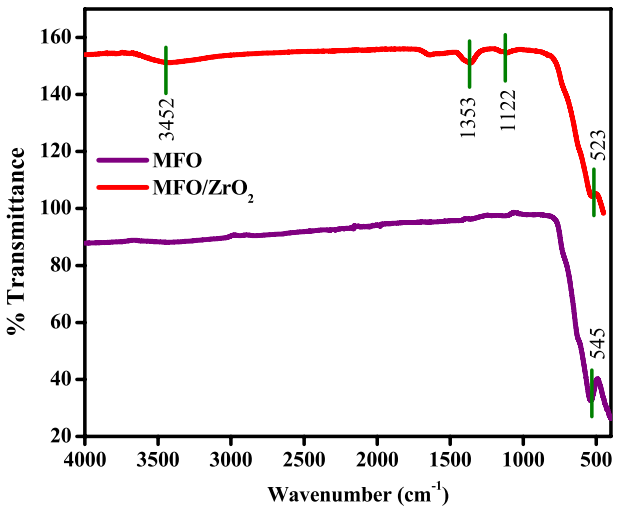

Fig. 4 FTIR spectra of MFO and MFO/ZrO2 NC at room temperature

the intrinsic stretching vibrations of the metal oxygen at the octahedral and tetrahedral sites, respectively [48]. The low intensity peaks observed at 1122, 1353 and 3452 cm^{-1} in MFO/ZrO_2 NC can be attributed to –CH, C=C and –CH_3, respectively [49].

3.1.4 UV–Visible diffuse reflectance spectroscopy (DRS)

UV–visible diffuse reflectance spectral (DRS) study has been carried out at room temperature, and band gap energy (E_g) was enumerated using Kubelka–Munk model. $[F(R)hv]^2$ against photon energy hv is plotted in Fig. 5. F(R) symbolizes the Kubelka–Munk function with

$$F(R) = \alpha = A = (1 - R)^2 / 2R \quad (3)$$

where R viewed diffuse reflectance in UV–Vis spectra. The band gap (E_g) of the material is evaluated by extrapolating straight line in the graph at $k = 0$ [50–53]. The band gap calculated for MFO and MFO/ZrO_2 was found to be 2.15 and 2.42 eV, respectively (Fig. 5 and Table 1). The band gap increases in the case of nanocomposite compared to host. The bands are produced by the integration of a large number of adjacent energy level atoms and molecules in the case of bulk matter. When the particle size attains the nanoscale, each particle is made up of a very few number of atoms or molecules, thereby reducing the number of overlapping orbitals or energy level, and the bandwidth becomes broadened. This phenomenon leads to an increased energy gap across the valence band and the conduction band. It results in the higher energy gap in nanocomposite than their corresponding bulk matter. In the present study, compared to host (2.15 eV), the composite MFO/ZrO_2 acquires a higher energy band gap (2.42 eV). The optical phonon energy was observed to be enhanced with the introduction of ZrO_2, as per the Burstein–Moss effect [54].

3.1.5 Electro-chemical impedance studies (EIS)

In order to get an idea about the effective separation of electron–hole pair and to estimate the charge transfer resistance, EIS is highly helpful. From the charge transfer resistance value, the photocatalytic activity of the synthesized samples can be analysed. The experiments were conducted with a usual three electrodes of the standard system with 0.1 M of NaOH electrolyte. Here,

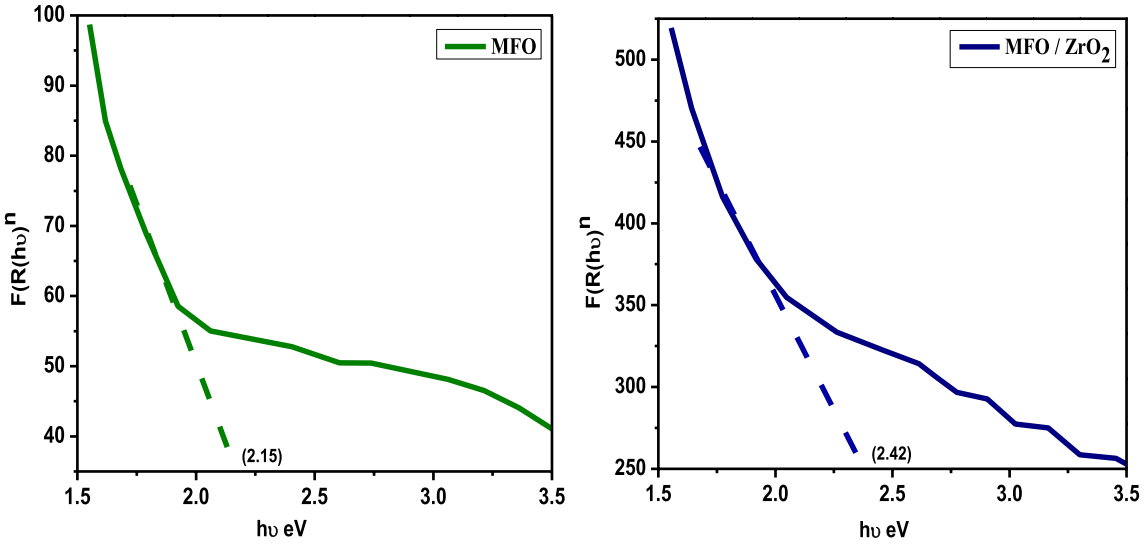

Fig. 5 Kubelka–Munk plot of MFO NP and MFO/ZrO_2 NC

counter electrode is the platinum electrode, Ag/AgCl acts as std. reference electrode, and the electrode prepared serves as an active electrode. The partial semicircle part and linear part indicate the high-frequency component and low-frequency component respectively, in impedance plot. As reported in the literature, if the diameter of semicircle is smaller in impedance plot, efficient separation of electron–hole pairs which are photogenerated takes place faster inter-facially [55].

The diameter of the semicircle for MFO NP and MFO/ZrO_2 NC was measured as 56 and 44 Ω, respectively. The charge transfer rate will be higher with smaller diameter of semicircle leading to lower rate of recombination of electron–hole pair with enhanced photocatalytic activity (Fig. 6). This result indicates that MFO/ZrO_2 with smaller diameter and high charge transfer rate will show enhanced photocatalytic activity compared to the synthesized MFO NP. These results were confirmed by UV–DRS studies which clearly show an increased band gap for MFO/ZrO_2NC.

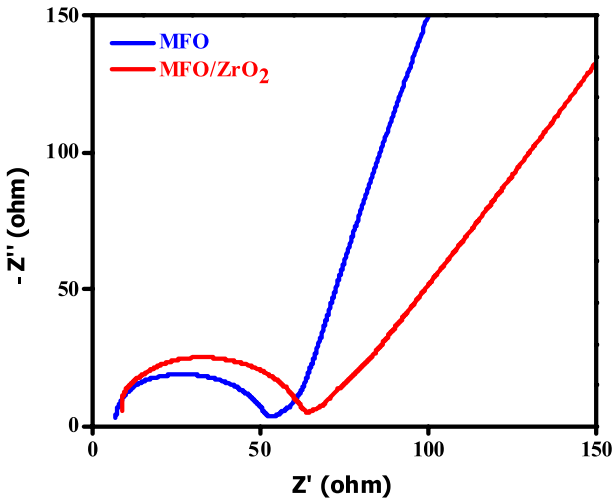

Fig. 6 Impedance plot for synthesized MFO NP and MFO/ZrO_2 NC

3.1.6 Photocatalytic studies

MB has been employed as a model pollutant to observe the decolourization using synthesized photocatalyst under sunlight irradiation. A stock solution of MB dye with an appropriate concentration has been prepared with double distilled water. From the prepared stock solution, 250 ml of dye solution has been made with required ppm and 20 ppm of MB dye solution loaded with 60 mg of the synthesized catalyst was taken in a glass trough and exposed to sunlight. The experiment was conducted at time 12 to 2 pm (in the month of April, Bangalore) with latitude (12.60 N) and longitude (77.31 E), respectively, along with an average solar intensity of about 0.736 kW m^{-2} as registered by solar radiometer. The sunlight was focussed on the glass trough using convex lens. The experiment has been carried out for synthesized MFO and MFO/ZrO_2 NC simultaneously to avoid any error that occurs because of fluctuations in sunlight.

Prior to the experimentation, the solution of the dye had to be kept in dark to maintain balanced equilibrium between adsorption and desorption process with the amount of dye lost during the process of adsorption, taken for consideration. After this process, the dye solution was transferred into trough with addition of photocatalyst and placed under sunlight irradiation. The suspension was continuously stirred using magnetic stirrer until complete

decolourization is attained. The dye solution (5 ml) was pipetted out on fixed time intervals from the glass trough till the completion of decolourization. The suspension pipetted out was centrifuged and analysed for the dye absorption before and after sunlight irradiation using UV–Vis spectrophotometer.

Figure 7a depicts the spectral absorbance and photodecolourization efficiency of MB over MFO/ZrO_2 NC as a function of irradiation time. When synthesized MFO was used as a photocatalyst, about 75% of MB was degraded within 90 min of irradiation time (Fig. 7b). But the decolourization of MB for MFO/ZrO_2 NC was found to be higher with 95% decolourization efficiency. It is notable that the simple adsorption efficiencies of MB for the prepared MFO and MFO/ZrO_2 samples in dark were found to be less than 5% (Fig. 7b), thereby clearly indicating a minute effect of MB adsorption on the efficiency of decolourization in the presently prepared photocatalyst.

The important evaluation criteria for photocatalyst are regeneration and recycling properties [19]. The experiment was conducted for five cyclic runs as exhibited in Fig. 7c. After the completion of first run, the photocatalyst was recovered using magnet, washed thoroughly using double distilled water, dried and used for further cycles. The same procedure was repeated after each cyclic run. The percentage of decolourization was found to be same for all the cycles performed, and the decrease in percentage of decolourization was found to be negligible after five cycles. Hence, it may be concluded that the photocatalyst was found to be photostable and could be utilized again.

3.1.7 Controlled decolourization and kinetic parameters

The adsorption and desorption properties on the photocatalyst surface in the photodecolourization process are influenced by pH [56]. To evaluate the pH factor on the activity of the catalyst, photocatalytic performance of

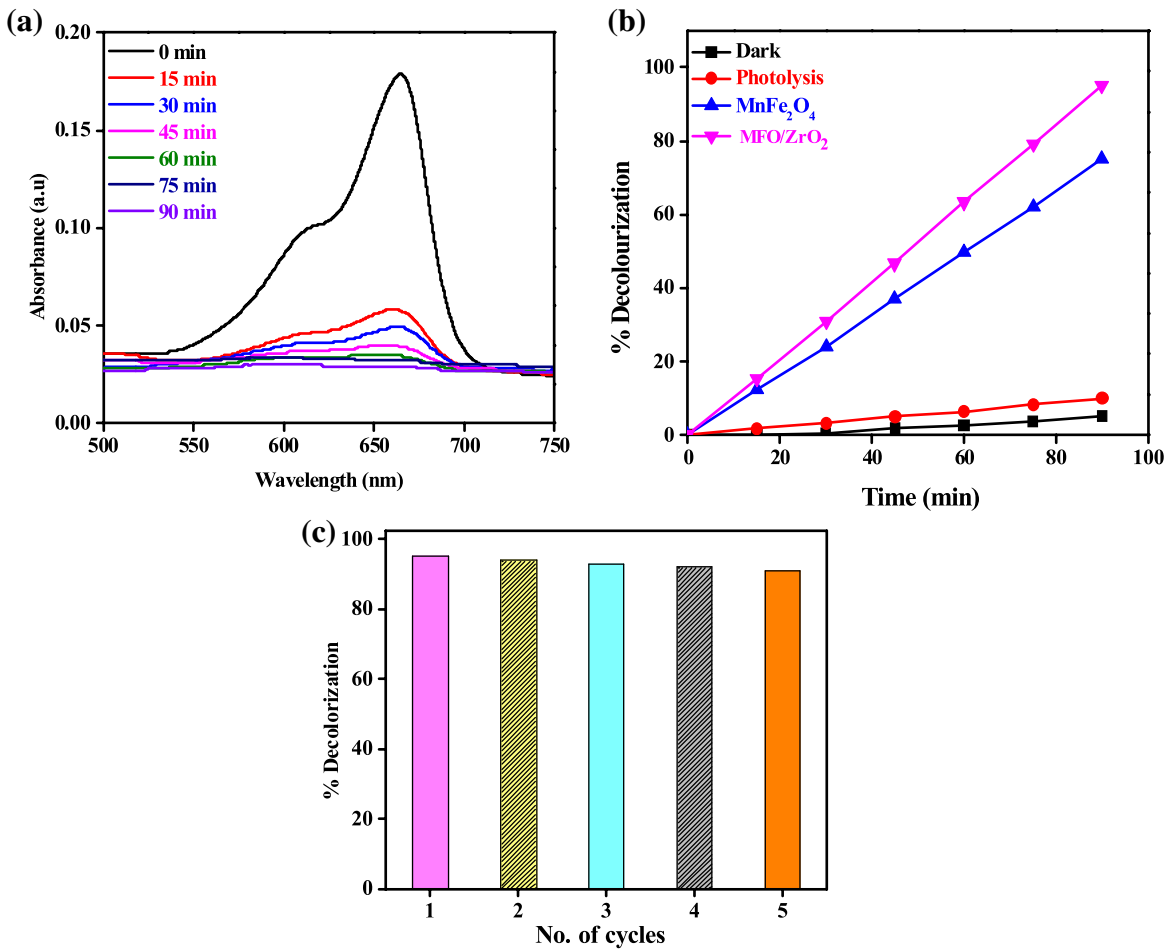

Fig. 7 **a** Spectral absorbance of MFO/ZrO_2 NC with the variation in irradiation time under sunlight for decolourization of MB; **b** % decolourization versus irradiation time of MB under sunlight irradiation for pure MFO and MFO/ZrO_2; **c** reusability of MFO/ZrO_2 NC for five consecutive cyclic runs

MB dye was observed in the range 3–11. At pH 1,3,5,7,9 and 11, the photocatalytic performance of MFO/ZrO_2 nanocomposite was found to be 43.65%, 60.14%, 81.35%, 95.14%, 89.32% and 70.57%, respectively (Fig. 8a).The obtained data demonstrate that at low and high pH values, photocatalytic performances are found to be low. At higher pH, high content of OH ion facilitates the separation of electron–hole pairs. However, CO_2 generated by light is trapped in the aqueous solution with carbonate and bicarbonate ions forming the alkaline medium. Carbonates are efficient scavengers of $^{\cdot}OH$ radicals owing to their very high rate constants with hydroxyl radicals $k = 3.9 \times 108\ M^{-1}\ s^{-1}$ for carbonate and $k = 8.5 \times 106\ M^{-1}\ s^{-1}$ for bicarbonate [57]. At very low pH, the acidic medium hampers the formation of $^{\cdot}OH$ radicals and consequently lowers the photocatalytic performance [58]. The rate constant at about pH 7 is $20.06 \times 10^{-3}\ min^{-1}$, and optimum pH value of this study is 7 for photocatalytic decolourization of MB.

The catalyst concentration is another crucial factor in the photocatalytic performance. The catalyst dosage was optimized by changing the amounts of MFO/ZrO_2 from 10 to 100 mg in MB dye solution. Photocatalytic performance increases with increasing catalyst dosage (Fig. 8b). A significant rise in rate constant is observed with an increment in the catalyst dose from 10 to 80 mg. However, the rate constant values for the 60 and 80 mg catalyst dose are relatively the same, and hence, 60 mg is assumed to be the optimum catalyst loading. For a catalyst dose of 10, 20, 40, 60, 80 and 100 mg, reaction rate constants are found to be 5.2×10^{-3}, 8.5×10^{-3}, 11.1×10^{-3}, 20.0×10^{-3}, 19.3×10^{-3}, $10.52 \times 10^{-3}\ min^{-1}$, respectively. The improved photocatalytic performance is ascribed to the enhanced photoactive sites on the surface of MFO/ZrO_2 photocatalyst, which boost the count of adsorbed photons and MB dye molecule adsorption. But, above the optimum photocatalyst dosage, the penetration depth of the photons decreased, hindering the photocatalyst efficiency [59].

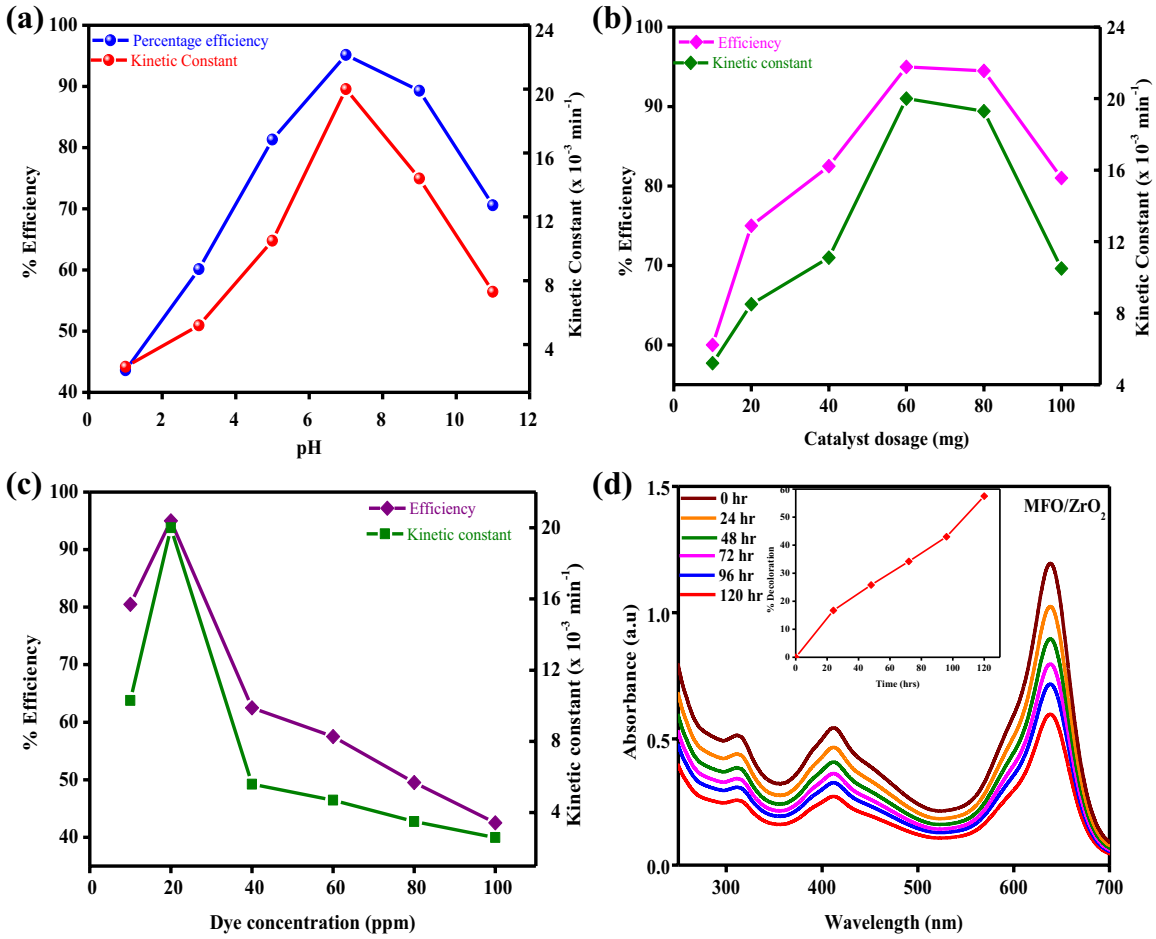

Fig. 8 Effect of **a** pH; **b** photocatalyst dose; **c** dye concentration on photocatalytic activity and variation in kinetic constant for dye decolourization; **d** the photocatalytic and kinetic rate constant for textile dye wastewater

The role of initial MB dye concentration at six different dye concentrations of 10, 20, 40, 60, 80 and 100 ppm was also studied for the MFO/ZrO_2 photocatalyst dose of 60 mg (Fig. 8c). As the concentration of MB dye increases from 10 to 100 ppm, the photocatalytic decolourization decreases from 95 to 42.5% within 90 min of sunlight irradiation. The active surface of the photocatalyst adsorbs industrially important MB dye molecules and reacts with photogenerated holes and hydroxyl radicals on the catalyst surface at low dye concentration which leads to effective photocatalytic performance. But, at high concentration of MB dye resulting in insufficient generation of charge carriers due to shielding of light by MB dye solution leads to reduced interaction with the MFO/ZrO_2 photocatalyst [60]. This results in the insufficient generation of hydroxyl radicals for the removal of high dye concentration. Further, the catalyst surface blocks the active sites due to overcrowding of MB dye molecules on the photocatalyst surface and decreases the production of $^{\cdot}OH$ radicals [61]. The rate constants of different dye concentrations are displayed in Fig. 8c. In the present study, an optimum MB dye concentration for catalytic decolourization is 20 ppm.

3.1.8 Textile wastewater treatment

The textile wastewater was collected from a textile manufacturer Sri Shilpanjali creation located at Hosakerehalli, Bengaluru. The textile wastewater possesses 8.37 pH along with chemical oxygen demand (COD) of 400 mg L^{-1} and 70 NTU turbidity. The different parameters such as pH, NTU turbidity and COD of collected wastewater sample are measured by standard protocols described by American Public Health Association [62].

The best photocatalyst MFO/ZrO_2 was employed to study the photocatalytic performance of industrial wastewater under sunlight. The textile wastewater was degraded under sunlight by following the similar procedure adopted for the decolourization of MB dye. The experiment was conducted for about 5 days. Every day the experiment was conducted with same set of photocatalyst but replenished wastewater. The spectral absorbance graph for MFO/ZrO_2 composite with the variation in irradiation time is represented in Fig. 8d. The photocatalyst showed decolourization efficiency of about 59% with the calculated rate constant value 1×10^{-4} min^{-1}(inset of Fig. 8d). The percentage decolourization of textile wastewater (59%) and rate constant value was found to be less compared to decolourization (95%) of MB dye. This may be due to the presence of mixture of dyes with different functional groups in industrial wastewater. Further, as the number and various types of organic pollutants increase in the textile wastewater, competition for the active sites also increases on the surface of catalyst, implying the cations or anions are eliminated based on their preferential discharge.

The presence of different functional groups in mixture of dyes influences the decolourization process which may lead to complicated mechanism [63]. COD (400 mg L^{-1}) and turbidity (70 NTU) of as-received water were found to be reduced to 110 mg L^{-1} and < 9 NTU in treated water. On exposure to sunlight for about 3 h, more than 72.5% COD and 87.1% turbidity present in the as-received water were reduced. Hence, it is observed that present composite MFO/ZrO_2 is an ideal supported photocatalyst for decolourization of textile wastewater under sunlight irradiation as it reduces turbidity and COD.

3.1.9 Photocatalytic mechanism

A probable photocatalytic mechanism for dye degradation of MFO/ZrO_2 nanocomposite has been projected and is demonstrated in Fig. 9. $MnFe_2O_4$ and ZrO_2 absorb the sunlight and generate electron–hole pairs (Eq. 4). The electrons keep shifting from $MnFe_2O_4$ to ZrO_2 till the Fermi level equilibrium is achieved for both. This type of transferring is due to the band potential of $MnFe_2O_4$ to be more negative than that of ZrO_2. The electrons generated on the surface of ZrO_2 react with absorbed oxygen, forming oxidants such as superoxide ions ($^{\cdot}O^{2-}$) (Eq. 5). Further, photoinduced holes from valence band (VB) of ZrO_2 immigrate to the less positive VB of $MnFe_2O_4$ and further react with water/^{-}OH ion (Eq. 6). The generated active species such as $^{\cdot}O^{2-}$, h^+ and $^{\cdot}OH$ by the above initiated process react to decolourize the dye molecules to CO_2, H_2O or other products (Eq. 7) [64–66].

The proposed mechanism of photocatalytic performance using $MnFe_2O_4/ZrO_2$ hetero-junction can be described as follows:

$$MnFe_2O_4/ZrO_2 + \text{Sunlight} \rightarrow e^-_{CB}\left(ZrO_2\right) + h^+_{VB}\left(MnFe_2O_4\right) \quad (4)$$

$$e^-_{CB} + O_2 \rightarrow {}^{\bullet}O_2 \quad (5)$$

$$h^+_{VB} + H_2O/OH^- \rightarrow {}^{\bullet}OH + H^+ \quad (6)$$

$$\text{MB or Industrial water} + {}^{\bullet}O^{2-}\left(h^+_{VB}, {}^{\bullet}OH\right) \rightarrow CO_2 + H_2O + \text{Other products} \quad (7)$$

Based on the above outcomes, the potential enhancement in the sunlight photocatalytic activity of $MnFe_2O_4/ZrO_2$ composite compared with that of $MnFe_2O_4$ can be attributed to: firstly, the existence of synergic effect between $MnFe_2O_4$ and ZrO_2 that leads to efficient separation of photogenerated electron–hole pairs and secondly,

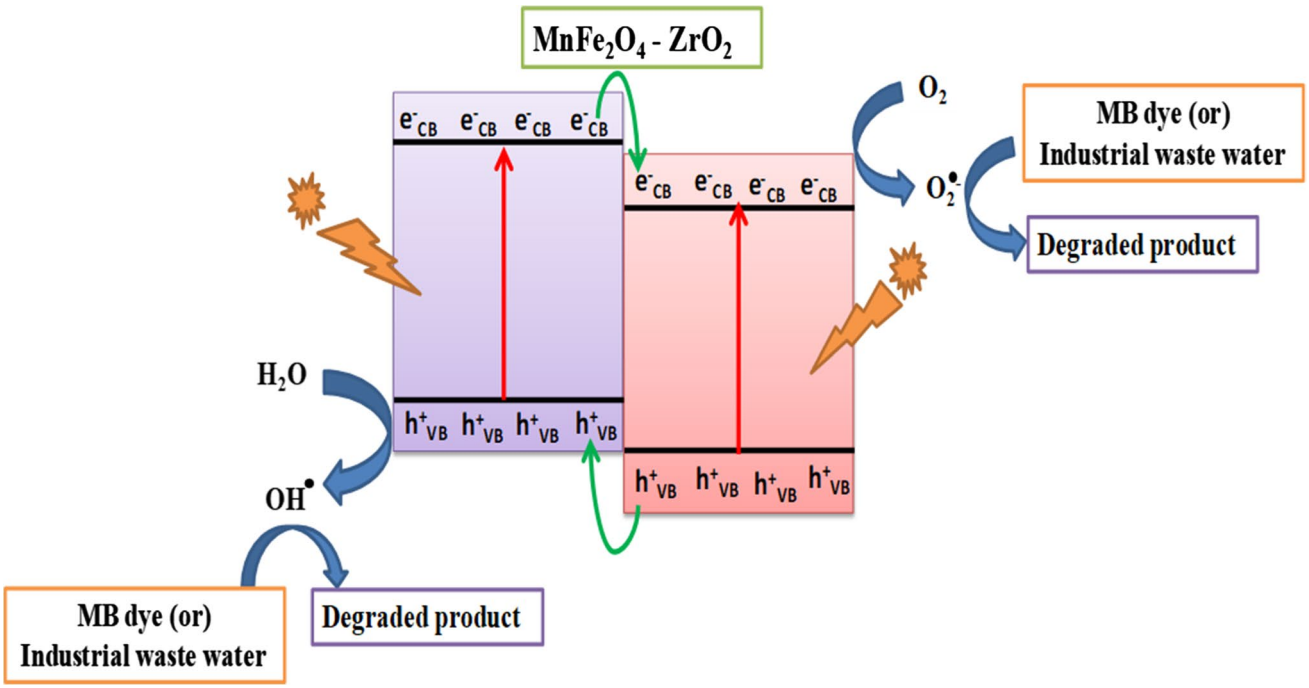

Fig. 9 Proposed sunlight photocatalytic mechanism for dye decolourization over MFO/ZrO_2 nanocomposite

the optimized parameters (crystallite size and broadened energy band), high crystallinity (PXRD), voids pores (SEM) and charge carrier recombination hindrance for the MFO/ZrO_2 nanocomposite results in the enhanced photocatalytic performance compared to synthesized MFO.

4 Conclusions

Magnetic nanocomposite MFO/ZrO_2 and synthesized MFO samples were successfully synthesized using convenient solution combustion method. Compared with the pure $MnFe_2O_4$, the $MnFe_2O_4$/ZrO_2 nanocomposite exhibited better photocatalytic activity to degrade MB under sunlight irradiation because of the existence of a synergic effect and interfacial interaction between $MnFe_2O_4$ and ZrO_2 that leads to efficient separation of electron–hole pairs and broadened light absorption of the composite compared to $MnFe_2O_4$. The structural properties from PXRD revealed the formation of spinel cubic and tetrahedral structure for synthesized NC without any additional peaks indicating the formation of NC. SEM image indicates the formation of agglomerated non-uniform structure with pores and voids. Furthermore, the MFO/ZrO_2 nanocatalyst could be easily separated from wastewater for reuse. As NC has enhanced photocatalytic activity towards MB dye decolourization and textile dye wastewater, it can be used as a potential candidate towards the wastewater treatment and environmental remediation.

Acknowledgements The author K.S. Anantha Raju thank VTU, TEQIP sponsored Competitive Research Grant (VTU/TEQIP 3/2019/321) and VGST, Govt. of Karnataka, India (No VGST/CESEM/2015-16), GRD No.-458 for sanctioning the research project.

Compliance with ethical standards

Conflict of interest The authors declare that they have no competing interests

References

1. Sun LS, Luo W (2013) Biochars prepared from anaerobic digestion residue, palm bark, and eucalyptus for adsorption of cationic methylene blue dye: characterization, equilibrium, and kinetic studies. Bioresour Technol 140:406–413
2. Yao Y, Xu F, Chen M, Xu Z, Zhu Z (2010) Adsorption behaviour of methylene blue on carbon nanotubes. Bioresour Technol 101:3040–3046
3. Li M, Qiang Z, Pulgarin C, Kiwi J (2016) Accelerated methylene blue (MB) degradation by Fenton reagent exposed to UV or VUV/UV light in an innovative micro photo-reactor. Appl Catal B Environ 187:83–89
4. Ali I, Asim M, Khan TA (2012) Low cost adsorbents for the removal of organic pollutants from wastewater. J Environ Manag 113:170–183

5. Panizza M, Cerisola G (2001) Removal of organic pollutants from industrial wastewater by electrogenerated Fenton's reagent. Water Res 35:3987–3992
6. Soltani N, Saion E, Hussein MZ, Erfani M, Abedini A, Bahmanrokh G, Navasery M, Vaziri P (2012) Visible light-induced degradation of methylene blue in the presence of photocatalytic ZnS and CdS nanoparticles. Int J Mol Sci 13:12242–12258
7. Adeleke JT, Theivasanthi T, Thiruppathi M, Swaminathan M, Akomolafe T, Alabic AB (2018) Photocatalytic degradation of methylene blue by ZnO/$NiFe_2O_4$ nanoparticles. Appl Surf Sci 455:195–200
8. Zhao X, Liu S, Tang Z, HongyunNiu Y, Meng W, Fengchang W, Giesy JP (2015) Synthesis of magnetic metal-organic framework (MOF) for efficient removal of organic dyes from water. Sci Rep 5:11849. https://doi.org/10.1038/srep11849
9. Awual MR, Yaita T, Shiwaku H (2013) Design a novel optical adsorbent for simultaneous ultra-trace cerium(III) detection, sorption and recovery. Chem Eng J 228:327–335
10. Awual MR, Hasan MM (2014) Novel conjugate adsorbent for visual detection and removal of toxic lead(II) ions from water. Microporous Mesoporous Mater. https://doi.org/10.1016/j.micromeso.2014.05.021
11. Awuala MR, Munjur MH, Khalequec MA (2015) Efficient selenium(IV) detection and removal from water bytailor-made novel conjugate adsorbent. Sensors Actuators B 209:194–202
12. Awual MR, Hasan MM, Znad H (2015) Organic–inorganic based nano-conjugate adsorbent for selective palladium(II) detection, separation and recovery. Chem Eng J 259:611–619
13. Awual MR (2016) Solid phase sensitive palladium (II) ions detection and recovery using ligand based efficient conjugate nanomaterials. Chem Eng J. https://doi.org/10.1016/j.cej.2016.04.071
14. Awual MR, Gaber E, Eldesoky TY, Naushad M, Shiwaku H, Alothman ZA, Suzuki S (2015) Schiff based ligand containing nanocomposite adsorbent for optical copper(II) ions removal from aqueous solutions. Chem Eng J 279:639–647
15. Awual MR (2019) Novel ligand functionalized composite material for efficient copper(II) capturing from wastewater sample. Compos B 172:387–396
16. Awual MR (2019) Efficient phosphate removal from water for controlling eutrophication using novel composite adsorbent. J Clean Prod 228:1311–1319
17. Awuala MR, Abdullah M, Asirib MM, Rahmanb NH (2019) AlharthicAssessment of enhanced nitrite removal and monitoring using ligand modified stable conjugate materials. Chem Eng J 363:64–72
18. Ren-BinWei Z-L, Guang-HuiGu Z, Zeng L, Chen Y, Liu Z-Q (2018) Dual-cocatalysts decorated rimous CdS spheres advancing highly-efficient visible-light photocatalytic hydrogen production. Appl Catal B 231:101–107
19. Li J-F, Zhong C-Y, Huang J-R, Chen Y, Wang Z, Liu Z-Q (2019) Carbon dots decorated three-dimensionally ordered macroporous-bismuth-doped titanium dioxide with efficient charge separation for high performance photocatalysis. J Colloid Interface Sci 553:758–767
20. Zheng N-C, Ouyang T, Chen Y, Wang Z, Chen D-Y, Liu Z-Q (2018) Ultrathin CdS shell-sensitized hollow S-doped CeO_2 spheres for efficient visible-light photocatalysis. Catal Sci Technol. https://doi.org/10.1039/c8cy02206b
21. Çalışkan Y, Yatmaz HC, Bektaş N (2017) Photocatalytic oxidation of high concentrated dye solutions enhanced by hydrodynamic cavitation in a pilot reactor. Process Saf Environ 111:428–438
22. Pelaez M, Nolan NT, Pillai SC, Seery MK, Falaras P, Kontos AG, Dunlop PSM, Hamilton JWJ, Byrne JA, O'Shea K, Entezari MH, Dionysiou DD (2012) A review on the visible light active titanium dioxide photocatalysts for environmental applications. Appl Catal B Environ 125:331–349
23. Teo SH, Islam A, Eng Seng Chan SY, Choong T, Nabeel H, Alharthi YH-Y, Awual MR (2019) Efficient biodiesel production from Jatropha curcus using $CaSO_4/Fe_2O_3$-SiO_2 core-shell magnetic nanoparticles. J Clean Prod 208:816–826
24. Manikandan A, Arul Antony S, Sridhar R, Bououdina M (2015) A simple combustion synthesis and optical studies of magnetic $Zn_{1-x}NixFe_2O_4$ nanostructures for photoelectrochemical applications. J Nanosci Nanotechnol 15:4948–4960
25. Chen D, Zhang Y, Kang Z (2013) A low temperature synthesis of $MnFe_2O_4$ nanocrystals by microwave-assisted ball-milling. Chem Eng J 215:235–239
26. Zhao DL, Lv Q, Shen ZM (2009) Fabrication and microwave absorbing properties of Ni–Zn spinel ferrites. J Alloys Compd 480:634–638
27. Reddy PAK, Srinivas B, ValluriDurgaKumari MV, Shankar MS, Lee JS (2014) $CaFe_2O_4$ sensitized hierarchical TiO_2 photo composite for hydrogen production under solar light irradiation. Chem Eng J 247:152–160
28. Jiang W, He J, Zhong J, Lu J, Yuan S, Liang B (2014) Preparation and photocatalytic performance of ZrO_2 nanotubes fabricated with anodization process. Appl Surf Sci 307:407–413
29. Tabrizi AG, Arsalani N, Mohammadi A, Namazi H, Ghadimia LS, Ahadzadeh I (2017) Facile synthesis of a $MnFe_2O_4$/rGO nanocomposite for an ultra-stable symmetric supercapacitor. R Soc Chem. https://doi.org/10.1039/c6nj04093d
30. Arief S, Jamarun N, Stiad Y (2017) Magnetically separable ZnO–$MnFe_2O_4$ nanocomposites synthesized in organic-free media for dye degradation under natural sunlight. Orient J Chem 33(6):2758–2765
31. Jalali MR, Salavati H, Goosheh AAR, Jeshvaghani AA (2018) Preparation and evaluation of optical properties of $MnFe_2O_4$/ZrO_2 nanocomposite. Int J Environ Sci Educ 13(3):265–274
32. VigneshaK SA, Min B-K, Kanga M (2014) Photocatalytic activity of magnetically recoverable$MnFe_2O_4$/g-C_3N_4/TiO_2nanocomposite under simulated solar light irradiation. J Mol Catal A Chem 395:373–383
33. Lv M, She X, Li Q, Sun J, Li H, Zhao XS, Guo P (2015) Synthesis of magnetic $MnFe_2O_4$/polyaniline composite microspheres and their electrocatalytic activity for oxygen reduction reaction. Sci Adv Mater 7(9):1686–1693
34. ur Rashid A, Humayun A, Manzoor S (2017) $MgFe_2O_4/ZrO_2$ composite nanoparticles for hyperthermia applications. J Magn Magn Mater 428:333–339
35. Baykal A, Deligoz H, Sozeri H, Durmus Z, Toprak MS (2012) Triethylene glycol stabilized $CoFe_2O_4$ nanoparticles. J Supercond Nov Magn 25:1879
36. Amir M, Sertkol M, Baykal A, Sozeri H (2015) Magnetic and catalytic properties of Cu_xFe_{1-x} Fe_2O_4 nanoparticles. J Supercond Nov Magn 28:2447
37. Baykal A, Durmus Z, Toprak MS, Sozeri H (2012) Synthesis and characterization of PEG-Sr hexaferrite by sol-gel conversion. J Supercond Nov Magn 25:2003
38. Shafiu S, Sozeri H, Baykal A (2014) Solvothermal synthesis of $SrFe_{12}O_{19}$ hexaferrites: without calcinations. J Supercond Nov Magn 27:1593
39. Valan MF, Manikandan A, Arul Antony S (2015) Microwave combustion synthesis and characterization studies of magnetic $Zn_{1-x}Cd_xFe_2O_4$ ($0 < x < 0.5$) nanoparticles. J Nanosci Nanotechnol 15:4543–4551
40. Renuka L, Anantharaju KS, Vidya YS, Nagaswarupa HP, Prashantha SC, Sharma SC, Nagabhushana H, Darshan GP (2017) A simple combustion method for the synthesis of multi-functional ZrO_2/CuO nanocomposites: excellent performance as sunlight

photocatalysts and enhanced latent fingerprint detection. Appl Catal B 210:97–115
41. Kulal SR, Khetre SS, Jagdale PN, Gurame VM, Waghmode DP, Kolekar GB, Sabale SR, Bamane SR (2012) Synthesis of Dy doped Co–Zn ferrite by sol–gel auto combustion method and its characterization. Mater Lett 84:169–172
42. Renuka L, Anantharaju KS, Sharma SC, Nagaswarupa HP, Prashantha SC, Nagabhushana H, Vidya YS (2016) Hollow microspheres Mg-doped ZrO_2 nanoparticles: green assisted synthesis and applications in photocatalysis and photoluminescence. J Alloys Compd 672:609–622
43. Li W, Wang X, Wang Z, Meng Y, Sun X, Yan T, You J, Kong D (2016) Relationship between crystalline phases and photocatalytic activities of $BiVO_4$. Mater Res Bull 83:259–267
44. Prasannakumar JB, Ramgopal G, Vidya YS, Anantharaju KS, Daruka Prasad B, Sharma SC, Prashantha SC, Premkumar HB, Nagabhushana H (2015) Bio-inspired synthesis of Y_2O_3: Eu^{3+} red nanophosphor for eco-friendly photocatalysis. J Spectrochim Acta 141:149–160
45. Vidya YS, Anantharaju KS, Nagabhushana H, Sharma SC, Nagaswarupa HP, Prashantha SC, Shivakumara C (2015) Combustion synthesized tetragonal ZrO_2: Eu^{3+} nanophosphors: structural and photoluminescence studies. J Spectrochim Acta 135:241–251
46. Kareema SH, Ooia YK, Abdulnoorb SS, Shamsuddinc M, Lee SL (2014) Influence of zinc on the structure and morphology of manganese ferrite nanoparticles. Jurnal Teknologi (Sci Eng) 69(5):103–106
47. Nagabhushana H, Nagabhushana BM, Kumar MM, Chikkahanumantharayappa MKR, Shivakumara C, Chakradhar RPS (2011) Synthesis, characterization and photoluminescence properties of CaSiO3:Eu^{3+} red phosphor. Spectrochim Acta Part A 78:64–69
48. KisanZipare J, Bandgar S, VikasMathe G (2015) Superparamagnetic manganese ferrite nanoparticles: synthesis and magnetic properties. J Nanosci Nanoeng 1:178–182
49. Venkataraju C, Pulsingh R (2014) FTIR and EPR studies of Nickel substituted nanostructured Mn Zn Ferrite. J Nanosci. https://doi.org/10.1155/2014/815385
50. Bouzidi A, Yahia IS, El-Sadek MSA (2017) Novel and highly stable indigo (C.I. Vat Blue I) organic semiconductor dye: crystal structure, optically diffused reflectance and the electrical conductivity/dielectric behaviors. Dyes Pigments 146:66–72
51. Senthilkumar V, Vickraman P, Ravikumar R (2010) Synthesis of fluorine doped tin oxide nanoparticles by sol–gel technique and their characterization. J Sol Gel Sci Technol 53:316
52. Chen Y, Liu B, Chen J, Tian L, Huang L, Tu M, Tan S (2015) Structure design and photocatalytic properties of one-dimensional SnO_2–TiO_2 composites. Nanoscale Res Lett 10:200
53. Yakuphanoglu F (2010) Electrical characterization and device characterization of ZnO micro ring shaped films by sol–gel method. J Alloys Compd 507:184–189
54. Guo H, Devakumar B, Vijayakumar R, Du P, Huang X (2018) A novel Sm3+ singly doped $LiCa_3ZnV_3O_{12}$ phosphor: a potential luminescent material for multifunctional applications. RSC Adv 8:33403–33413
55. Ali HAM, El-Nahass MM, El-Zaidia EFM (2018) Optical and dispersion properties of thermally deposited phenol red thin films. Optic Laser Technol 107:402–407
56. Awual MR (2019) A facile composite material for enhanced cadmium (II) ion capturing from Wastewater. J Environ Chem Eng 7:103378
57. Borji S, Nasseri S, Mahvi AH, Nabizadeh R, Javadi AH (2014) Investigation of photocatalytic degradation of phenol by Fe(III)-doped TiO_2 and TiO_2 nanoparticles. J Environ Health Sci Eng 12:101–110
58. Avasarala BK, TirukkovalluriS R, Bojja S (2011) Photocatalytic degradation of monocrotophos pesticide—an endocrine disruptor by magnesium doped titania. J Hazard Mater 186:1234–1240
59. He Z, Shi Y, Gao C, Wen L, Chen J, Song S (2014) BiOCl/$BiVO_4$ p–n heterojunction with enhanced photocatalytic activity under visible-light irradiation. J Phys Chem C 118:389–396
60. Sun D, Li J, He L, Zhao B, Wang T, Li R, Yin S, Feng Z, Sato T (2014) Facile solvothermal synthesis of BiOCl–TiO_2 heterostructures with enhanced photocatalytic activity. CrystEngComm 16:7564–7574
61. Asilturk M, Sayilkan F, Arpac E (2009) Effect of Fe^{3+} ion doping to TiO_2 on the photocatalytic degradation of Malachite Green dye under UV and vis-irradiation. J Photochem Photobiol 203:64–71
62. Standard Methods for the Examination of Water and Wastewater (1995) 19th Edition, American Public Health Association Inc., New York
63. Danwittayakul S, MayureeJaisai J (2015) Efficient solar photocatalytic degradation of textile wastewater using ZnO/ZTO composites. Appl Catal B Environ 163:1–8
64. Schneider JJ, Naumann M (2014) Template-directed synthesis and characterization of microstructured ceramic Ce/ZrO_2@SiO_2 composite tubes. J Nanotechnol 5:1152–1159
65. Wang J, Huang J, Meng J, Li Q, Yang J (2016) Double-hole codoped huge-gap semiconductor ZrO_2 for visible-light photocatalysis. Phys Chem Chem Phys 18:17517–17524
66. Thejaswini TVL, Prabhakaran D, Maheswari MA (2017) Synthesis of mesoporous worm-like ZrO_2–TiO_2 monoliths and their photocatalytic applications towards organic dye degradation.J. Photochem Photobiol A344:212–222